Influence of specimen dimensions and strain measurement methods on tensile stress–strain curves

Y.H. Zhao [a,*], Y.Z. Guo [b,c], Q. Wei [b,**], T.D. Topping [a], A.M. Dangelewicz [d], Y.T. Zhu [e], T.G. Langdon [f,g], E.J. Lavernia [a]

[a] Department of Chemical Engineering and Materials Science, University of California at Davis, Davis, CA 95616, USA
[b] Department of Mechanical Engineering, University of North Carolina at Charlotte, Charlotte, NC 28223, USA
[c] NW Polytech University, Sch Aeronaut, Xian 710072, PR China
[d] Los Alamos National Laboratory, Los Alamos, NM 87545, USA
[e] Department of Materials Science and Engineering, North Carolina State University, Raleigh, NC 27695-7919, USA
[f] Departments of Aerospace & Mechanical Engineering and Materials Science, University of Southern California, Los Angeles, CA 90089-1453, USA
[g] Materials Research Group, School of Engineering Sciences, University of Southampton, Southampton SO17 1BJ, UK

ARTICLE INFO

ABSTRACT

Miniature tensile specimens, having various sizes and geometries, are often used to measure the mechanical properties of bulk nanostructured materials. However, these samples are generally too small for use with conventional extensometers so that the strains are usually calculated from the crosshead displacements. This study uses experimental results and finite element modeling (FEM) to critically evaluate the influence of the specimen dimensions and strain measurement methods on the tensile curves obtained from miniature specimens. Using coarse-grained Cu as a model material, the results demonstrate that the values of strain obtained from the crosshead displacement are critically influenced by the specimen dimensions such that the uniform elongation and the post-necking elongation both increase with decreasing gauge length and increasing specimen thickness. The results provide guidance on the optimum procedures for the tensile testing of miniature specimens of both coarse-grained and nanostructured materials.

© 2009 Elsevier B.V. All rights reserved.

1. Introduction

The numerous reports of super-high strength for various nanostructured (NS, structural features <100 nm) metals and alloys continue to attract interest from the scientific and technical communities. It is evident, however, that a significant obstacle obstructing the widespread engineering application of this class of materials lies in their generally poor ductility [1–4]. Inspection of the scientific literature shows numerous recent efforts directed towards developing strategies for improving the ductility of these materials and these strategies have met with varying degrees of success [5–15]. A review of the published experimental results reveals that the ductility is frequently measured using non-standardized mechanical testing incorporating miniature dog-bone tensile specimens having different sizes and geometries that are not in conformity with ASTM standards [16]. Thus, the thickness of some of these nanostructured tensile specimens vary from about

100 μm [10,11] or even about 10 μm [17] to several millimeters [8,9,12–15] and the gauge lengths vary from 1 mm [18–21] to several millimeters [8–15,17] or even several centimeters [22] where these various dimensions depend primarily upon the availability of material.

On the basis of ASTM standards, a subsize rectangular tensile specimen should have a gauge length of 25 mm, a width of 6 mm, a thickness smaller than 6 mm and a radius fillet of 6 mm. An important requirement is that the ratio of gauge length to width should be maintained at 4. In the case of tensile specimens with circular cross-sections, the ratio of gauge length to gauge diameter should be 5 and the fillet radius should equal the gauge diameter. In practice, the ratio of gauge length to thickness/diameter used in NS materials is frequently smaller than 4. Moreover, because of the small dimensions of the gauge lengths, the strains of the miniature specimens are often derived from the crosshead displacements due to the difficulties in attaching strain gauges or applying extensometers [18–21]. As a consequence of these variations, it is not surprising that published results for bulk NS materials are often difficult to interpret in terms of the underlying mechanisms (ductility, for example) and they invariably pose a challenge in any attempts to reproduce the data.

* Corresponding author. Tel.: +1 530 7529568; fax: +1 530 7529554.
** Corresponding author. Tel.: +1 704 6878213.
E-mail addresses: yhzhao@ucdavis.edu (Y.H. Zhao), qwei@uncc.edu (Q. Wei).

It follows from these differences that it is necessary to ask whether the geometries/dimensions of the dog-bone specimens and the strain values determined from crosshead displacements are factors that influence the experimental results. To date, the only possible comparisons between materials are based on directly comparing the reported data without considering any possible sample size effects [3,4,7]. However, an understanding of the precise effect of specimen dimensions is an important prerequisite not only in interpreting mechanical behavior but also in the design and implementation of materials for use as miniature components and devices in advanced engineering applications such as digital cameras, mobile phones, mini-robots, micro-electro-mechanical systems (MEMS), miniature medical devices and biotechnological or chemical processing equipment [23–27].

A survey of the literature reveals an evident size effect in the mechanical behavior of materials when testing in compression [28–32], tension [33–42], indentation [43] or torsion [44]. An increase in yield strength and a decrease in tensile ductility with decreasing specimen thickness were reported in freestanding Cu, Al, Au and Ni foils with thicknesses below 250 μm or even in the sub-micrometer regime [38–42]. Moreover, molecular dynamics (MD) simulations of Cu nanowires indicate that the yield stress decreases while ductility increases with increasing nanowire diameter due to the enhanced opportunities for dislocation motion at the larger sizes [35]. Room temperature tensile results obtained with single crystal Cu samples (with diameters between 0.5 and 8 μm) showed that the strain hardening was negligible for long gauge specimens but pronounced for short gauge specimens where dislocation glide was constrained due to sample geometry [36]. However, the thickness in these foils was below 250 μm or even in the sub-micrometer regime [38–42]. The variety of size effects reported in the literature indicates that various physical deformation mechanisms, operating on different length scales, govern the mechanical behavior of materials [45–50]. Therefore, it is probable that the specimen thickness effects reported in these studies cannot be extended to macroscopic NS tensile specimens where the specimen thickness is larger than 100 μm. Furthermore, the gauge length of the standard ASTM tensile specimen affects only the post-necking strain and not the portion of the stress–strain curve prior to necking but for specimens deviating from ASTM standard geometries the influence of gauge length remains to be established.

In recent studies it was demonstrated, using both experiments and finite element modeling (FEM), that apparent tensile specimen dimension/geometry effects are significant in the case of ultrafine grained (UFG) Cu [51]. Specifically, it was reported that the post-necking elongation increases significantly with increasing specimen thickness and decreasing gauge length. The thickness effect is caused primarily by the necking geometry and fracture modes whereas the gauge length effect originates from the strain definition. With a decrease in thickness, the gauge part is effectively transformed from a bulk to a sheet geometry and the stress state within the gauge changes from a more or less bi-axial condition to a uni-axial stress state under tension, thereby resulting in a change from diffuse necking to localized necking [52–54]. However, in this study it was difficult to reveal any effects from specimen dimensions and strain measurement methods on the uniform elongation because there was essentially an absence of any uniform elongation in the UFG Cu [51]. Other investigators have reported that ductility increases with increasing specimen thickness and decreasing gauge length [55–58] but there are no systematic analyses of these trends.

In the present study, we critically evaluate the possible influences of strain measurement methods and specimen dimensions on both the uniform elongation and the post-necking elongation behavior. We used coarse-grained (CG) Cu for this study because its large uniform elongation makes it easier to study the size effect before the onset of necking. First, we investigate the effects of specimen thickness and gauge length via experimentation combined with FEM, with the strain values established on the basis of crosshead displacement. Second, we establish the influence of specimen geometry on tensile results via FEM with the strain values established based on the actual gauge elongation. Although no experimental measurements of strain from the gauge section were performed in this study, the FEM analysis of the strains measured from the gauge section is valid and sufficient to give information on the effects of the strain measurement methods on the stress–strain curves. In practice, it will be shown that the stress–strain curves predicted by FEM agree well with those measured experimentally for strains determined from the crosshead displacements. Finally we analyze the experimental errors in strain measurements from the crosshead displacement and discuss the origins of specimen dimension effects. Our overall objective is to recommend guidelines regarding the experimental characterization of mechanical properties using small-scale samples.
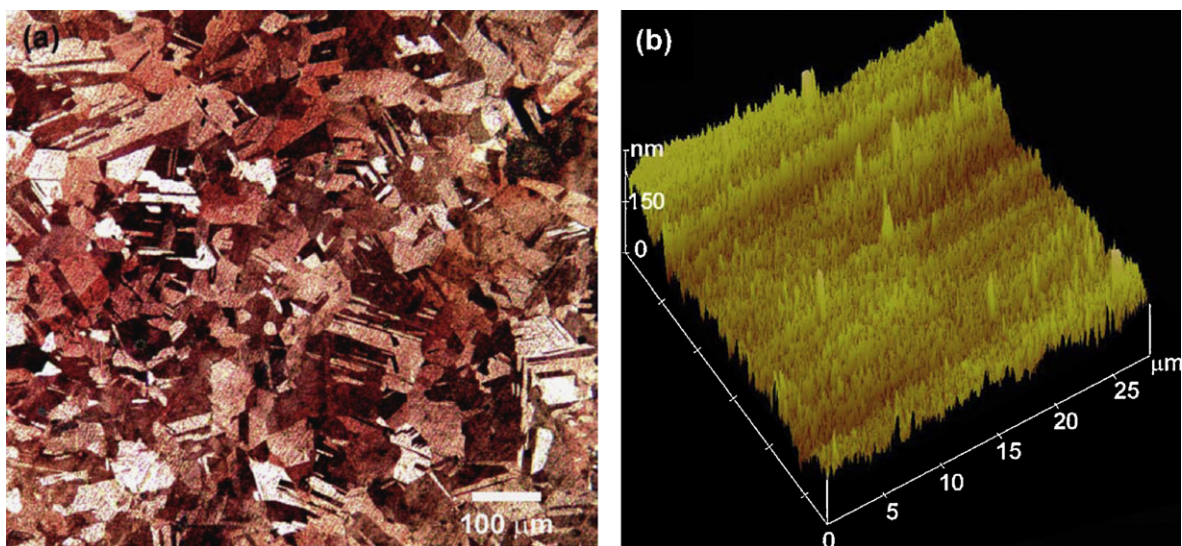

Fig. 1. (a) Optical metallographic image of the Cu sample showing coarse grains decorated with a high density of annealing twins. (b) Surface topography of the tensile specimen of the Cu showing a surface root mean square (RMS) roughness of about 50 nm, as measured by atomic force microscopy (AFM).
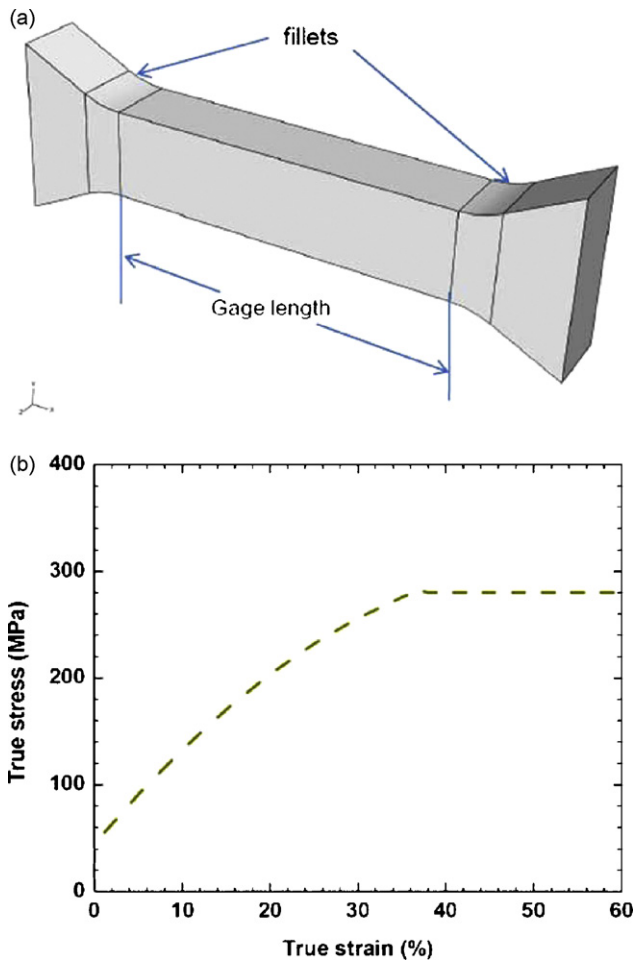
Fig. 2. (a) Dog-bone specimen model used to simulate the geometric effects on the measured stress–strain behavior under nominally uni-axial tension. In this model, the width is fixed at 2.0 mm, and the size of the fillets is fixed at 3.0 mm (curvature radius). (b) Stress–strain behavior of the simulated material. The material is assumed to exhibit bi-linear constitutive behavior.
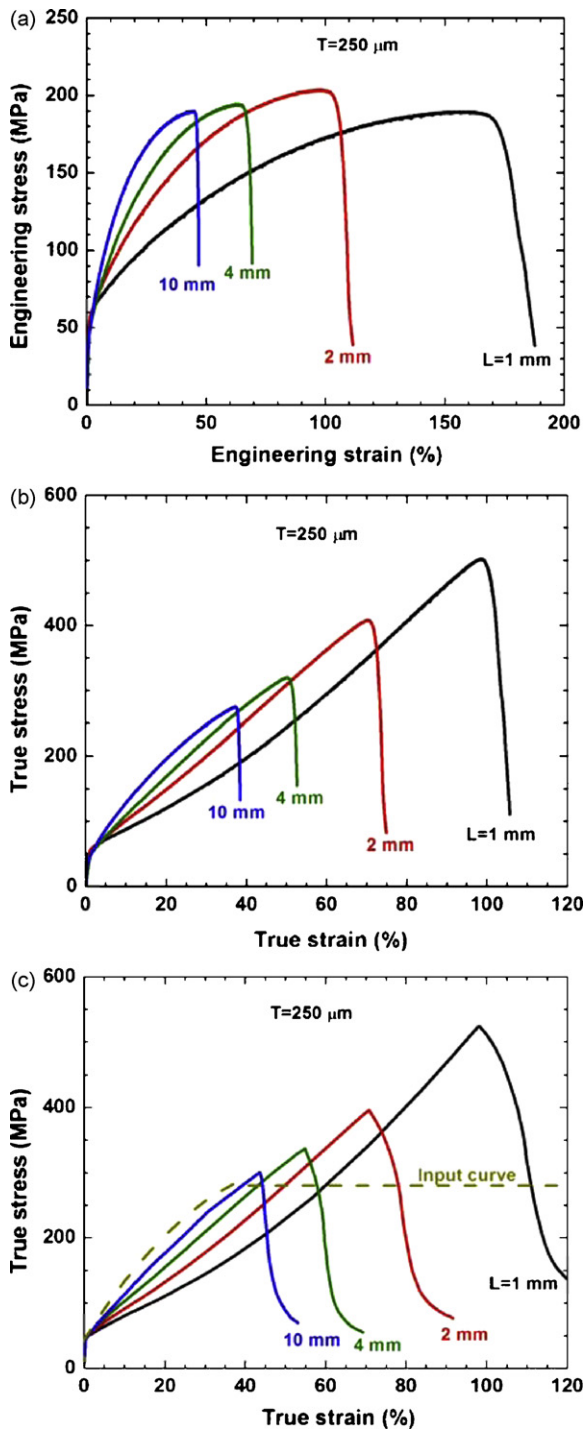
2. Experimental

The as-received pure copper (99.99%) rod was annealed at 500 °C for 3 h in an argon atmosphere to promote the formation of a coarse grain structure with an average grain size of about 50 μm as established by optical metallographic analyses and shown in Fig. 1a. A high density of annealing twins, with spacings ranging from several micrometers to tens of micrometers, was observed within these coarse grains. Flat dog-bone specimens with different dimensions were then sectioned using electro-discharge machining (EDM). In this study, we studied a range of specimen dimensions. First, the specimen thickness (T) was varied from ~250 μm to ~2.0 mm while the gauge length (L) and width (W) were maintained constant at 1.0 and 2.0 mm, respectively. Second, L was varied from 1.0 to 10.0 mm and T and W were maintained constant at 250 μm and 2.0 mm, respectively. Two sets of samples were prepared for every combination of T and L in order to ensure reproducibility of results. The radius of the fillets of all specimens was maintained at 3 mm. The flat surfaces of the dog-bone specimens were polished using SiC papers with a final FEPA standard grit size of 4000 to yield a surface root mean square (RMS) roughness of about 50 nm as measured by atomic force microscopy (AFM) and shown in Fig. 1b. Tensile tests were performed using a Shimadzu Universal Tester with an initial quasi-static strain rate of 1.0×10^{-3} s^{-1}. Measurements of strain were derived based on the crosshead displacements.
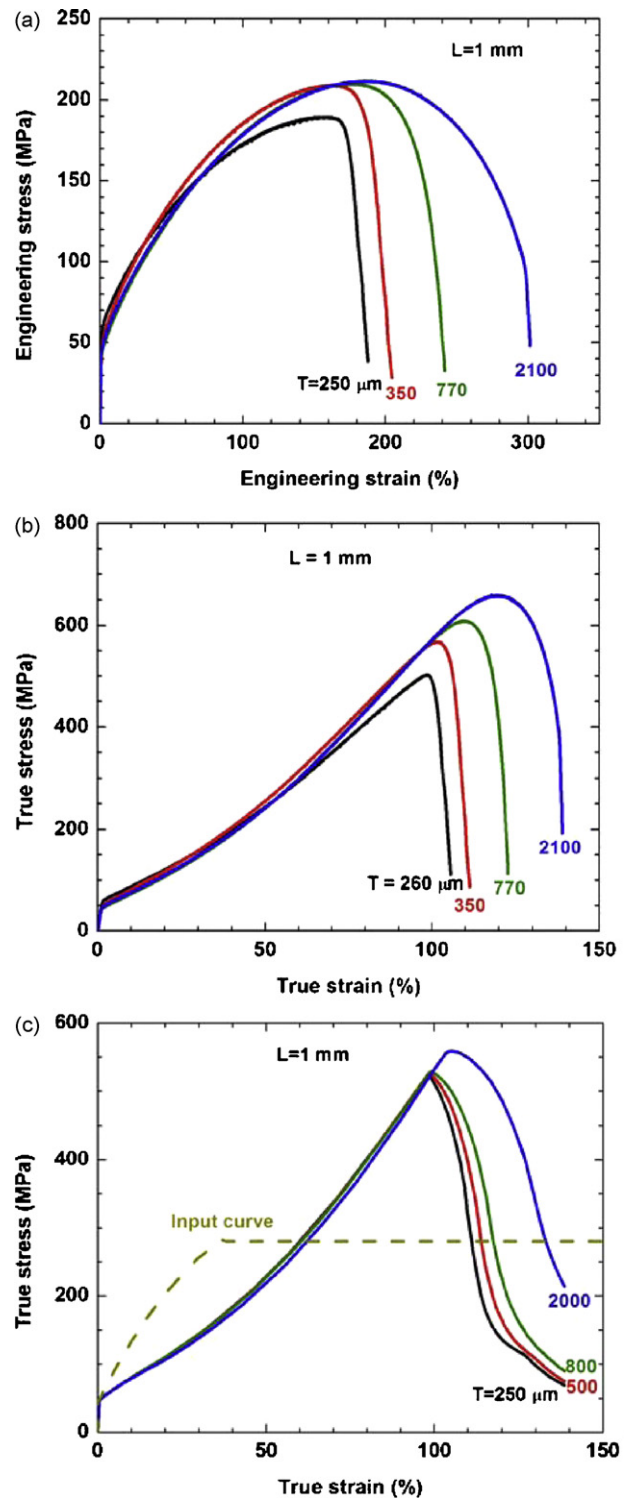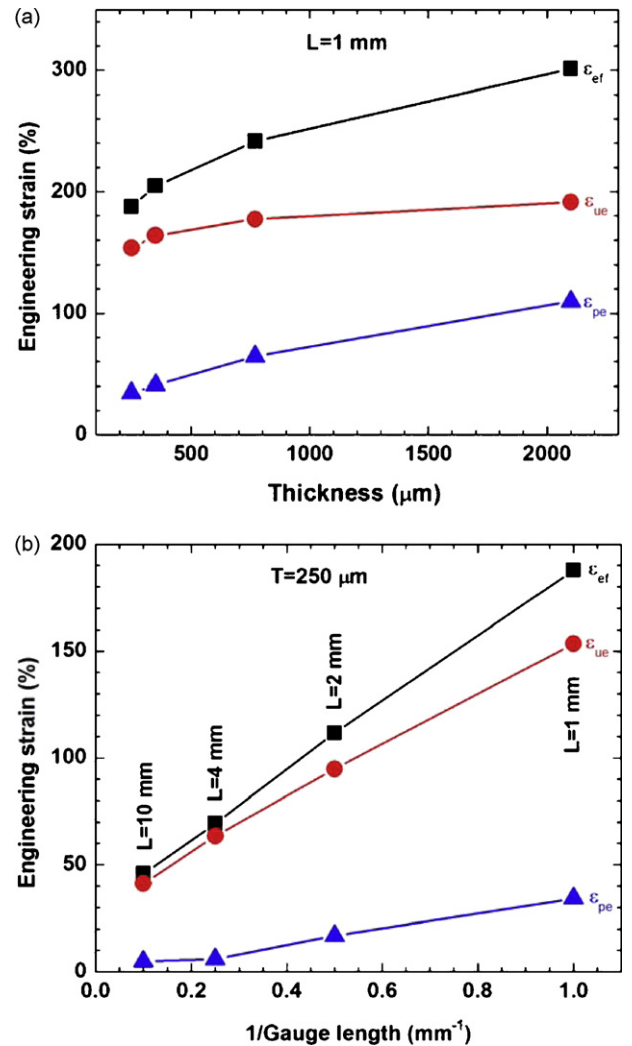

Fig. 3. Experimental (a and b) and FEM simulated (c) tensile stress–strain curves of coarse-grained Cu showing the thickness T effect. The tensile specimens have a gauge length L of 1 mm. The different thicknesses are indicated in the figures. The true stress–strain curves (b) were transferred from the engineering stress–strain curves (a). The input stress–strain curve in FEM simulation was indicated by a dashed line in part (c).

In parallel with the experimental analysis, FEM was used to simulate the effect of specimen size/geometry and the strain measurement method on the tensile behavior of dog-bone specimens under nominally uni-axial tension. The dog-bone specimen model used for the FEM simulations is shown in Fig. 2a. In this model, the

Fig. 4. Experimental (a and b) and FEM simulated (c) tensile stress–strain curves of coarse-grained Cu showing the gauge length L effect. The tensile specimens have a thickness T of 250 μm. The different values of L are indicated in the figures.

Fig. 5. Thickness T (a) and gauge length L (b) effects on elongation to failure ε_{ef}, uniform elongation ε_{ue} and post-necking elongation ε_{pe} of the CG Cu with $L = 1$ mm and $T = 250$ μm, respectively, as indicated in the figures.

measured experimentally. This ideal bi-linear material was used as the input for the FEM modeling and we assumed that the left end of the specimen was fixed with a velocity load applied to the right end. In this study we compared two ways of measuring elongation of the specimen Δl: using the crosshead displacement as in the experiments and using the gauge length elongation.

The ABAQUS software was used to perform the FEM simulations. The surface topography of the tensile specimens was established using a Nanoscope®IIIa Scanning Probe Microscope operating in a tapping mode. The fracture surface observations were performed using an FEI XL-30 SFEG Scanning Electron Microscopy (SEM) operating at a voltage of 25 kV.

3. Results

3.1. Strain derived from crosshead displacement

3.1.1. The results in tension

Fig. 3 shows the experimentally measured engineering (Fig. 3a) and true (Fig. 3b) stress–true strain curves as well as the FEM simulated true stress–true strain curves (Fig. 3c) of the Cu samples with the strain derived from the crosshead displacement with an L of 1.0 mm and, as indicated, different values of T. The experimental true stress–strain curves (Fig. 3b) were trans-

width is fixed at 2.0 mm and the fillet or curvature radius is 3.0 mm for all samples. Four gauge lengths of 1.0, 2.0, 4.0 and 10.0 mm were investigated at a constant T of 250 μm and four specimen widths of 250, 500, 800 and 2000 μm were investigated at a constant L of 1.0 mm. In order to maintain the analysis tractable, we considered a material of ideal bi-linear constitutive behavior with the stress–strain curve displayed by Fig. 2b. The yield strength of the model material was taken as 44 MPa with an elastic modulus of 110 GPa, and a strain-hardening modulus, representing the slope of the second plastic portion of the stress–strain curve, of 100 MPa as

Table 1
The thickness T effect on uniform elongation ε_{ue}, the post-necking elongation ε_{pe} and elongation to failure ε_{ef} of the CG Cu.

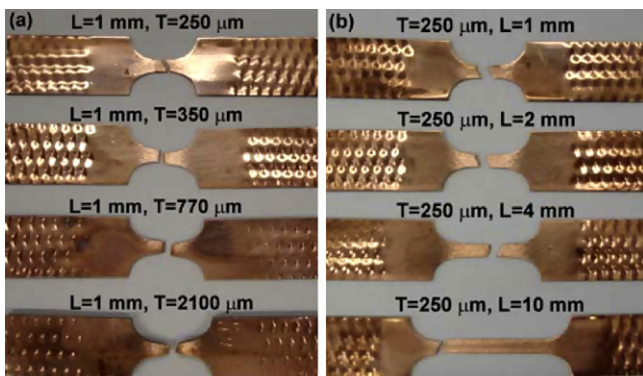| T (μm)	ε_{ef} (%)	ε_{pe} (%)	ε_{ef} (%)
250	188	34	154
350	205	41	164
770	241	64	177
2100	302	110	192

Table 2
The gauge length L effect on uniform elongation ε_{ue}, the post-necking elongation ε_{pe} and elongation to failure ε_{ef} of the CG Cu.

L (mm)	L^{-1} (mm^{-1})	ε_{ef} (%)	ε_{pe} (%)	ε_{ue} (%)
1	1	188	34	154
2	0.5	112	17	95
4	0.25	69	6	63
10	0.1	46	5	41

Table 3
The thickness T effect on shear fracture angle θ and area reduction RA of Cu.

| T (μm)	θ (°)	A (%)
250	58	90
350	85	91
770	83	95
2100	81	96

Table 4
The gauge length L effect on shear fracture angle θ and area reduction RA of Cu.

L (mm)	L^{-1} (mm^{-1})	θ (°)	A (%)
1	1	58	90
2	0.5	62	93
4	0.25	65	91
10	0.1	59	93

ferred from the engineering stress–strain curves (Fig. 3a). For all samples, both experimental and FEM simulation revealed large uniform deformation accompanied by evident strain hardening in the CG Cu in tension leading to a large overall tensile ductility or elongation to failure. This behavior is typical for coarse-grained face-centered cubic (f.c.c.) metals due to their high dislocation storage capability. Specifically, with increasing thickness both the necking portion (post-necking elongation) and the strain-hardening part (uniform elongation) in the stress–strain curves of the CG Cu are prolonged to a higher strain resulting in a larger overall ductility (Fig. 3a and b). However, there is no thickness effect on the yield strength or the strain-hardening rate of Cu within the thickness range studied in these experiments. All samples have yield strengths of about 44 MPa and similar strain-hardening rates. The results of the FEM simulations reveal thickness effects which correspond closely to those observed experimentally (Fig. 3c).

The gauge length effects on the experimental engineering (4a) and true (4b) stress–strain curves and the FEM simulated true stress–strain curves (4c) of CG Cu with a T of 250 μm are shown in Fig. 4. A reduction in gauge length prolongs the stress–strain curves to higher fracture strains or higher apparent ductility primarily by prolonging the uniform elongations. Moreover, with decreasing L, the rate of strain hardening decreases. However, the yield strength remains independent of L with a constant value of about 44 MPa for all samples. It is evident that the FEM simulations and the experimental results are consistent with each other.
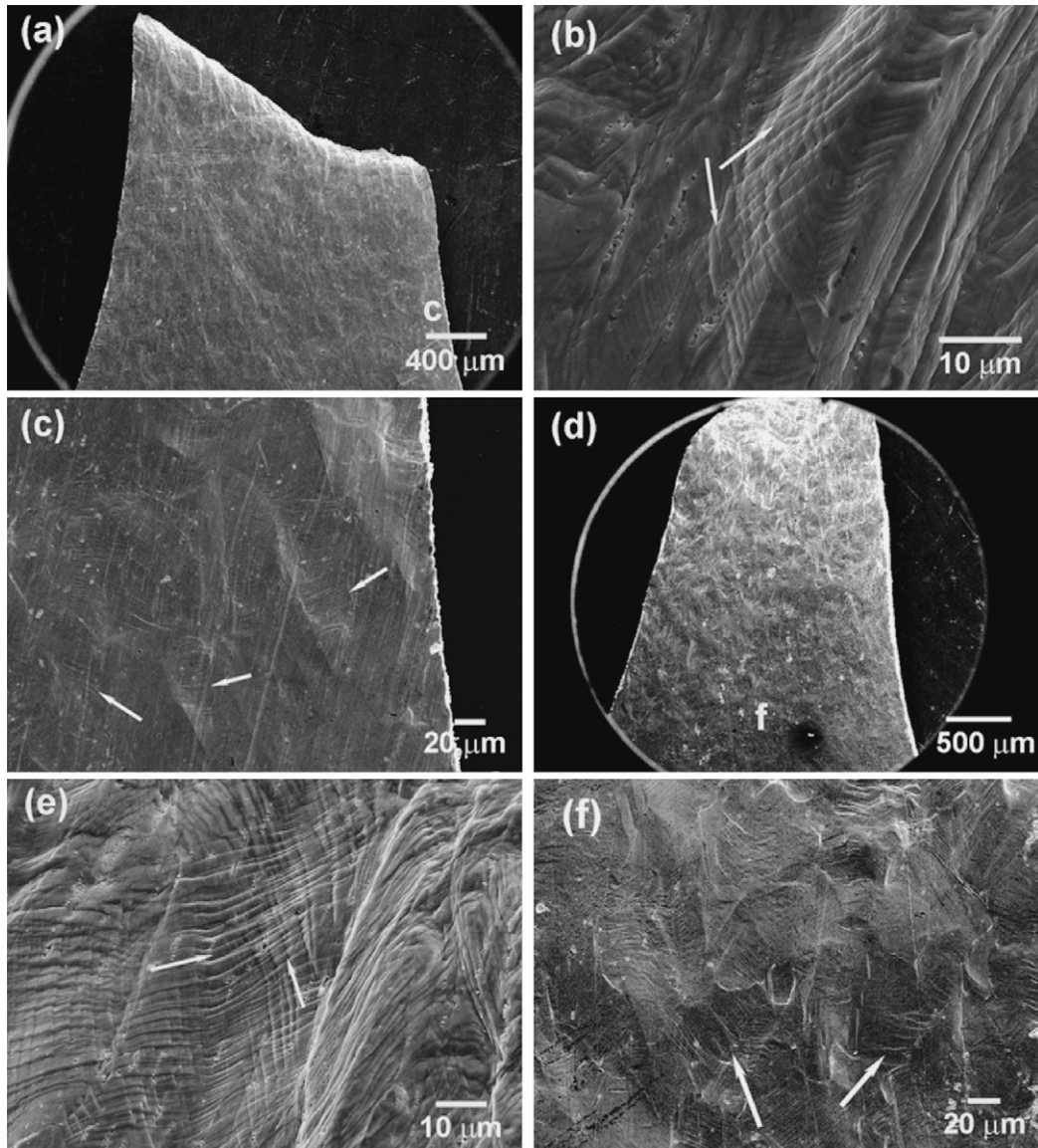
The uniform elongation ε_{ue} can be determined using the Considère's criterion [53] governing the onset of localized deformation:

$$\left(\frac{\partial \sigma}{\partial \varepsilon}\right)_{\dot{\varepsilon}} = \sigma \tag{1}$$

The elongation to failure ε_{ef}, ε_{ue} and the post-necking elongation ε_{pe} (= $\varepsilon_{ef} - \varepsilon_{ue}$) of CG Cu are shown in Fig. 5a and b as a function of T and L and listed in Tables 1 and 2, respectively. From Fig. 5a, the effect of specimen thickness (T) on elongation to failure can be principally attributed to its effect on the post-necking component.
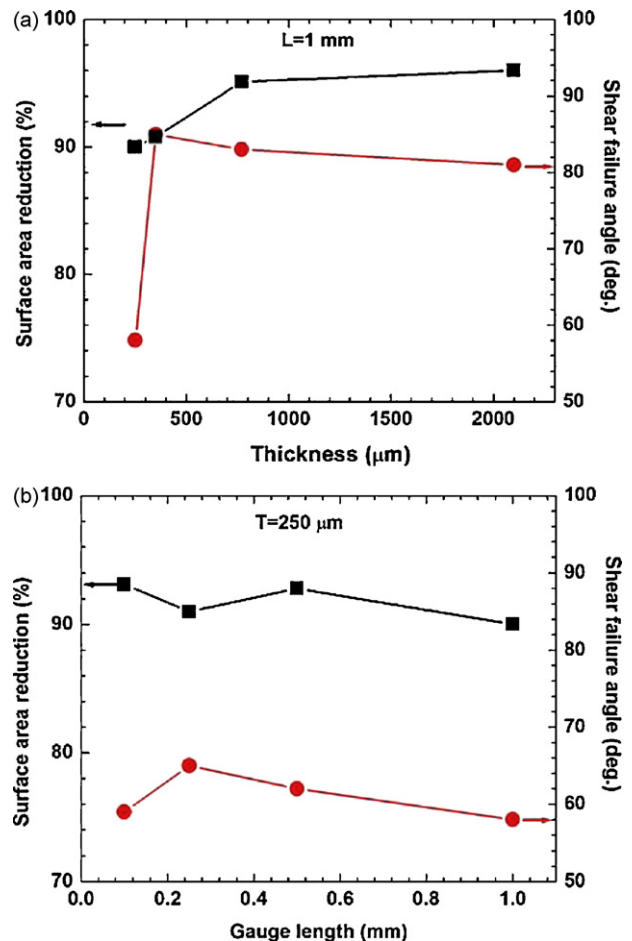
Fig. 7. Thickness (a) and gauge length (b) effects on fracture surface area reduction and shear failure angle of the CG Cu with L = 1 mm and T = 250 μm, respectively, as indicated in the figures.

Fig. 6. Tensile fractured specimens with L = 1 mm and different thicknesses (a), and T = 250 μm and different gauge lengths (b), as indicated in the figures.

Fig. 8. SEM images of the fracture orientations of the CG Cu with L = 1 mm and T = 250 μm (a–c), and with L = 1 mm and T = 2100 μm (d–f), respectively. (b) and (e) are magnified images of (a) and (b) near fracture, respectively. (c) and (f) are magnified images of (a) and (b) near gauge corner parts marked by "c" and "f", respectively. Evident deformation is found to occur in the gauge corner parts.

By increasing T from 250 μm to 2100 μm, ε_{pe} increases significantly from 34 to 110%, and ε_{ue} increases from 154 to 192% resulting in an overall increase in ε_{ef} from 188 to 302%. However, from Fig. 5b the variation of the uniform elongation versus L reveals a dominant contribution to the overall variation of the elongation to failure. By decreasing L from 10 to 1 mm, ε_{ef} is increased from 46 to 188% with a dominant contribution from ε_{ue} (increased from 41 to 154%) and a minor contribution from ε_{pe} (increased from 5 to 34%). All values of ε_{ef}, ε_{ue} and ε_{pe} reveal a consistent proportional relationships with L^{-1}.
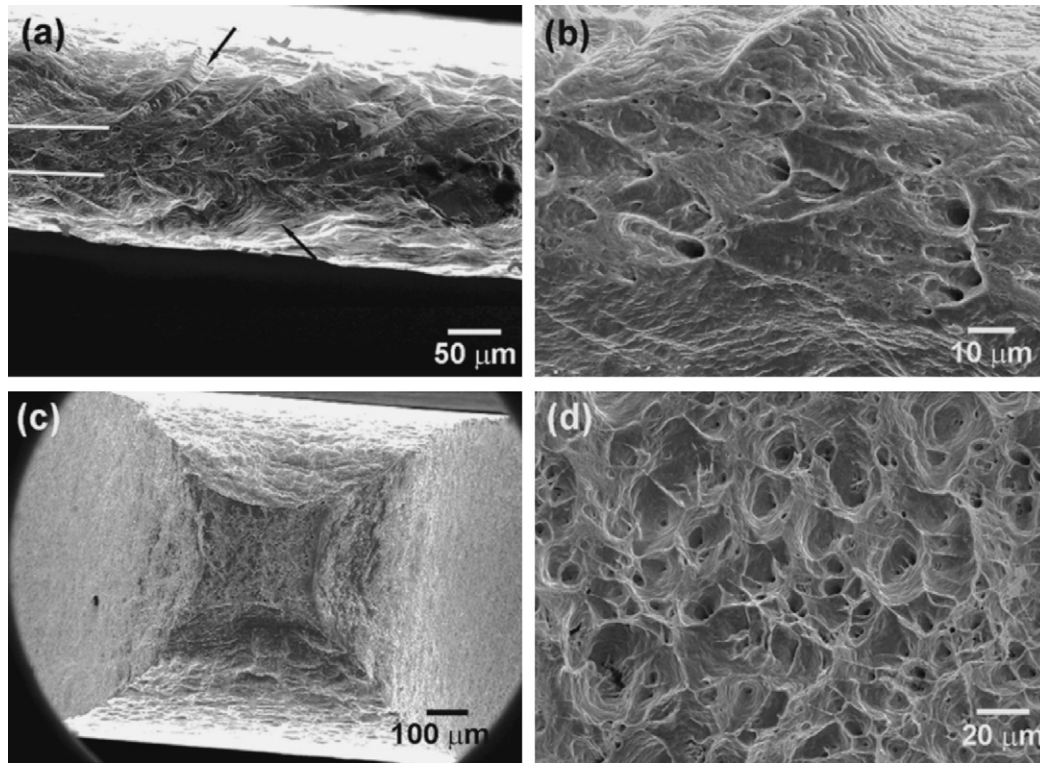
3.1.2. The fracture surface morphology and fracture mode

In order to understand the above specimen size and geometry effects on the tensile behavior of the CG Cu, it is necessary to critically examine the failure characteristics. Fig. 6 shows the tensile fractured samples with L = 1 mm and different values of T (Fig. 6a) and with T = 250 μm and different values of L (Fig. 6b). From Fig. 6a it is seen that the specimen thickness critically influences the fracture mode. With increasing thickness, the fracture mode of the CG

Cu changes from shear to normal tensile fracture. However, from Fig. 6b it is seen that the gauge length has no apparent influence on the shear fracture mode of the CG Cu with T of 250 μm.

We also performed detailed SEM observations on the size effect of the fracture mode as well as the fracture surfaces. The T and L effects on the shear fracture angle, θ, between the fracture plane and the loading axis are plotted in Fig. 7 from the SEM observations and they are listed in Tables 3 and 4, respectively. It is evident that the shear fracture angle increases from $58°$ to $85°$ with increasing T from 250 to 350 μm (Fig. 7a) but thereafter it remains unchanged with increasing T up to a value of 2.1 mm. On the other hand, θ remains constant at approximately 58–$65°$ when L varies from 1 to 10 mm with T = 250 μm (Fig. 7b). These results demonstrate that thinner samples are more susceptible to shear failure and that the gauge length has no evident influence on the failure mode.

Fig. 8 shows some typical side-view SEM images of fractured tensile specimens at different magnifications with L = 1 mm and T = 250 μm (Fig. 8a–c) and with L = 1 mm and T = 2.1 mm (Fig. 8d–f), respectively. It is evident that, with the exception of the shear frac-

Fig. 9. SEM images of the fracture surfaces of the CG Cu with $L = 1$ mm and $T = 250\ \mu$m (a and b), and $L = 1$ mm and $T = 2100\ \mu$m (c and d), respectively. (b) and (d) are magnified images of (a) and (b) to show dimple size and morphology in the fracture surfaces, respectively.

tures (Fig. 8a), the pre-polished specimen surfaces become irregular after tension and the extent of the surface irregularities increase with increasing T and in areas closer to the fracture point (Fig. 8a and d). Multiple slip bands are visible at high magnifications with band-to-band distances of several micrometers from areas near the fracture point (Fig. 8b and e) to the gauge corners (Fig. 8c and f), as highlighted by the arrows. The original equiaxed grains with an average size of about 50 μm are elongated significantly upon plastic deformation by slip and, in addition, different grains with different orientations coalesce giving rise to uneven surfaces. The rougher surfaces in the thicker specimens suggest a larger deformation, where this is consistent with the measured higher ductilities.

The T and L effects on the surface area reduction, $RA\%$, as obtained from SEM results are also plotted in Fig. 7 and listed in Tables 3 and 4, respectively. It is evident that $RA\%$ increases slightly from 90 to 96% by increasing T from 250 to 2100 μm (Fig. 7a) whereas $RA\%$ remains unchanged at approximately 90–93% when L varies from 1 to 10 mm and $T = 250$ μm (Fig. 7b). These results suggest that thicker samples are susceptible to necking and a larger $RA\%$ value but the gauge length has no evident influence on the necking behavior.

Fig. 9 shows typical SEM images of the fracture surfaces of the tensile specimens with $L = 1$ mm and $T = 250$ μm (a and b) and $L = 1$ mm and $T = 2.1$ mm (c and d), respectively. It appears that the change in tendency towards necking with T originates from specimen geometry or more specifically from the T/W ratio. For thin, sheet-like specimens where T/W is small, necking occurs primarily along the direction of T (Fig. 9a); but when T/W is close to unity or T is comparable to W, necking occurs in both the W and T directions (Fig. 9c). A close examination of the SEM images indicates that when $T = 2.1$ mm necking reduces the thickness and the width by 80% resulting in an $RA\%$ of 96%. When $T = 250$ μm, necking reduces the thickness by 87% but the width only by about 25% to give a value for the $RA\%$ of 90%. Large necking at $T = 2.1$ mm leads to a rougher cross-sectional surface and a larger necking length in the tensile direction (Fig. 8a and c), giving rise to a prolonged

post-necking strain in the stress–strain curves (Fig. 3). Fig. 9b and d shows the magnified fracture surfaces for specimens with $L = 1$ mm and $T = 250$ μm and $L = 1$ mm and $T = 2.1$ mm, respectively. Elongated dimples are observed in thinner specimens caused by shear fracture in contrast with the rounded dimples in thicker specimens as a result of normal fracture.

3.2. The strain measured from the gauge section

From the above experimental and FEM results, it is apparent that the strain derived from the crosshead displacement is significant affected by the specimen dimensions (both thickness and gauge length). It is usually considered that the gauge length of ASTM standard tensile specimen affects only the post-necking elongation and hence there should be no influence on the uniform elongation prior to necking. Therefore, it is possible that the experimental effects of specimen dimensions on uniform elongation may be caused by an error in strain on the basis of the crosshead displacement. To clarify this problem, FEM simulations were undertaken to establish the effect of the specimen dimensions using strain values determined from the gauge length elongations.

Fig. 10 shows the FEM results of the thickness T effect on the true stress–strain curves of the CG Cu with the strain measured from the gauge length elongation with $L = 1$ mm. It is apparent that the uniform elongation is independent of T and, furthermore, that T has influence only on the post-necking elongation. The error $(\varepsilon_{CH} - \varepsilon_{GE})/\varepsilon_{GE}$ in the strain measurement based on the crosshead displacement (ε_{CH}) relative to that from the gauge length elongation (ε_{GE}) is shown in Fig. 10(b) and it is apparent that the error may be as large as four times the value of ε_{GE}.

Fig. 11 shows the FEM results of the effects of the gauge length L on the true stress–strain curves of CG Cu with the strain measured by the gauge length elongation and $T = 250$ μm. These plots show that the uniform elongation is also independent of L and, as with T, L influences only the post-necking elongation. Fig. 11(b) shows
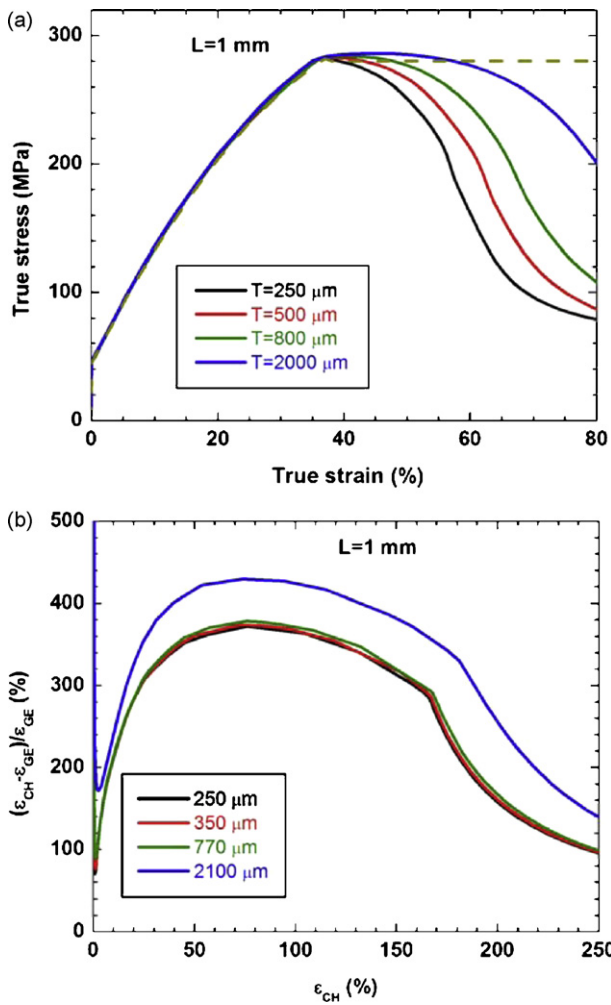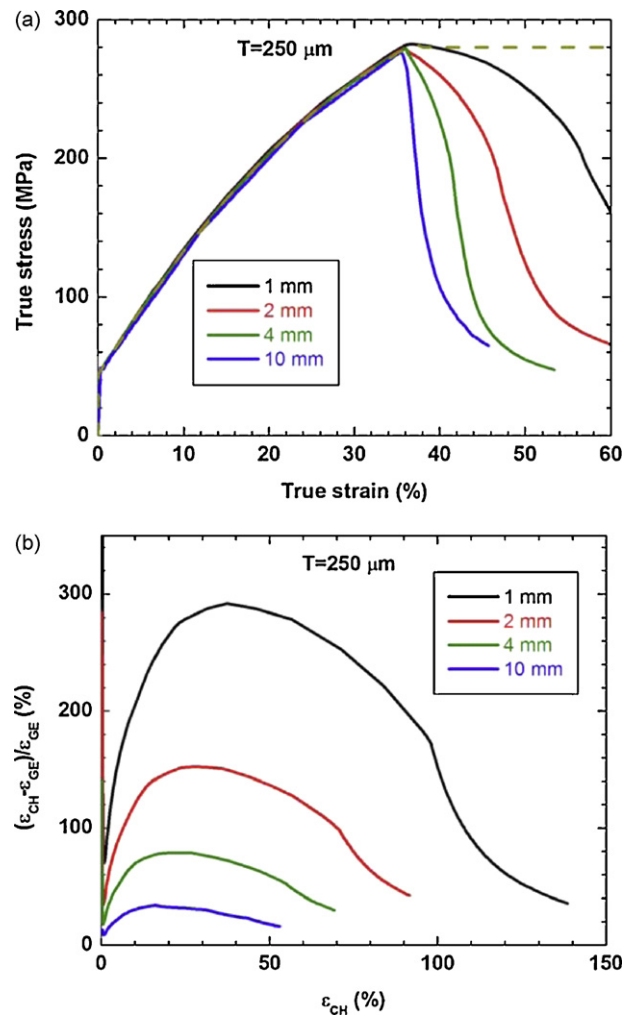
Fig. 10. (a) FEM simulated results of the thickness T effect on true stress–strain curves of the CG Cu with strain measured by gauge length elongation and $L = 1$ mm. The different thicknesses are indicated in the figure. (b) Error $(\varepsilon_{CH} - \varepsilon_{GE})/\varepsilon_{GE}$ of using crosshead displacement to calculate strain ε_{CH} compared with using gauge length elongation to calculate strain ε_{GE}.

Fig. 11. (a) FEM simulated results of the gauge length L effect on true stress–strain curves of the CG Cu with strain measured by gauge length elongation and $T = 250$ μm. The different gauge lengths are indicated in the figure. (b) Error $(\varepsilon_{CH} - \varepsilon_{GE})/\varepsilon_{GE}$ of using crosshead displacement to calculate strain ε_{CH} compared with using gauge length elongation to calculate strain ε_{GE}.

the error $(\varepsilon_{CH} - \varepsilon_{GE})/\varepsilon_{GE}$ for using ε_{CH} compared with using ε_{GE}. Thus, the error increases with decreasing L and may be as large as three times the value of ε_{GE}. Nevertheless, even for the situation of $L = 10$ mm, the error remains at about 10% of ε_{GE}.

4. Discussion

4.1. Strain measurements using the gauge length elongation

On the basis of the above results, if the strain is determined using the gauge length elongation, the specimen thickness and the gauge length affect only the post-necking elongation which increases with increasing T and decreasing L. The effect of T may be explained by a change in the failure mode of the CG Cu specimens as a function of specimen thickness and this may be further understood with assistance from the FEM results shown in Fig. 12. When specimens with $L = 1.0$ mm are pulled to an engineering strain of about 175%, one pair of conjugated localized shear bands appears at the gauge center of the sheet-like specimen (T/W ratio very small) as shown in Fig. 12(a). When T is 250 μm, the shear band-like structures combine to form a singular shear band on the upper plane of the gauge section as illustrated in Fig. 12(b). The shear angle with respect to the tensile direction is about 50°, agreeing approximately with the experimental value of ~58° for CG Cu with $T = 250$ μm. From the

equivalent plastic strain (PEEQ) distribution at the side plane of the gauge region, it is seen that shear deformation occurs only in the upper plane of the gauge section. However, when T is equal to 800 and 2000 μm, shear deformation is also observed on the side plane of the gauge region as shown in Fig. 12(c) and (d). The interaction of the two series of shear bands at the upper and side planes
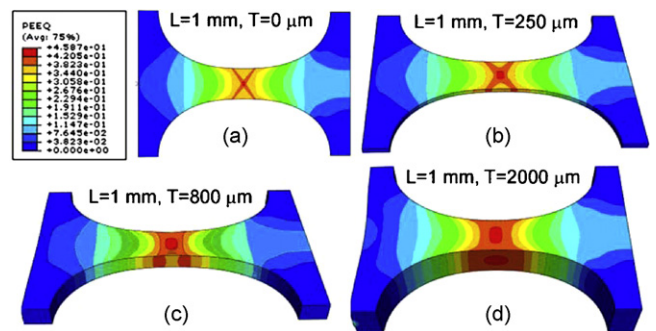
Fig. 12. FEM results on thickness (a–d) effects on the equivalent plastic strain (PEEQ) distribution in the specimens. Parts (a)–(d) show the PEEQ distributions of the specimens with $L = 1$ mm and T equals to 0, 250, 800 and 2000 μm at about 175% engineering strain.
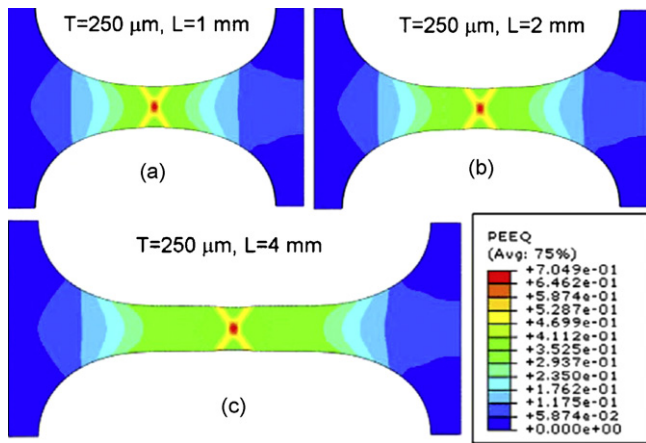
Fig. 13. FEM results on gauge length (a–c) effects on the equivalent plastic strain (PEEQ) distribution at the specimens. Parts (a)–(c) show the PEEQ distributions of the specimens with $T = 250\,\mu m$ and gauge lengths of 1, 2 and 4 mm at a maximum PEEQ of about 0.7.

leads to a more complex stress state within the thicker specimens, thereby giving rise to the experimentally observed normal fracture mode.

These observations agree well with the SEM observations on the fracture mode and fracture surface morphology as shown in Figs. 6–9. In addition to the specimen geometry limitation on the necking response, the presence of surface defects, such as surface roughness and a localized deformation layer caused by grinding, may also contribute to the thickness effect in both the uniform and post-necking strain. This is because the proportional influence of the surface layer increases with decreasing thickness. For the CG Cu, the decreased number of grain layers across the thickness direction may also contribute to the thickness effect because the large grain size of 50 μm is comparable to the small specimen thickness.

The gauge length effect on the post-necking elongation may be explained using the definition of the contributions to the total elongation Δl that defines the engineering strain:

$$\Delta l = \Delta l_1 + \Delta l_2 + \Delta l_3 \tag{2}$$

where Δl_1 is the elastic elongation, Δl_2 the uniform plastic elongation and Δl_3 the plastic elongation by necking. For the CG Cu, the contributions from Δl_1 are usually negligible. The post-loading SEM observations suggest that the gauge length has no evident effect on the failure mode and necking process, as further verified by the FEM results shown in Fig. 13. The necking area is about 2.0 mm in width which is the same as the width of the specimen. These results imply that Δl_3 is independent of gauge length. Therefore, the post-necking component $\Delta l_3/l_0$ is inversely proportional to initial gauge length l_0. This is further confirmed on the basis of the results shown in Fig. 5b. Both ε_{ef} and ε_{pe} of the CG Cu exhibit linear relationships with l_0^{-1}. By extrapolating the ε_{pe} and ε_{ef} versus l_0^{-1} curves to $l_0^{-1} = 0$, it is found that $\varepsilon_{pe} \approx 0$ and $\varepsilon_{ef} \approx 30\%\,(\varepsilon_{ue})$. This means that an infinite l_0 tends to nullify the post-necking strain so that the failure strain is then equal to the uniform strain.

4.2. The error in strain from the crosshead displacement

The preceding results show that the strain derived from the cross-head displacement shows a significant dimensional influence on the uniform elongation of the CG Cu: specifically, the uniform elongation increases with decreasing gauge length and increasing specimen thickness. However, FEM simulations verify that this effect of the specimen dimension on the uniform elongation is caused by the error in the strain measurement. This error in the

measured global strain has two sources: one is from the machine compliance of the loading frame, Δl_4, and the other is from the deformation of the gauge corner region, Δl_5, so that Eq. (2) is replaced with

$$\Delta l = \Delta l_1 + \Delta l_2 + \Delta l_3 + \Delta l_4 + \Delta l_5 \tag{3}$$

As shown in Fig. 8, the specimen surface at the gauge corner region also becomes rough and at higher magnification multi-slip events occur in the corner part (Fig. 8c and f). This is further confirmed by the FEM results in Figs. 12 and 13. Relatively high PEEQ strain is also identified in the corner region. The strain contribution from the deformation of the gauge corner region (with elongation Δl_5) should be increased with increasing thickness, resulting in an increased uniform elongation versus thickness (Fig. 3). It is noted that Δl_4 is a constant for a given machine and material (CG Cu) and increasing the gauge length can mitigate the strain error and cause a decrease in uniform elongation with increasing gauge length (Fig. 4).

It is evident that strain measurements can be accurately established by using extensometers of various types. For small samples, special techniques based on laser interferometry have been developed [59,60]. Alternative methods include the application of a digital image correlation (DIC) technique which is now becoming increasingly popular in experimental micro-/nano-mechanics [61]. The advantage of DIC resides in its dynamic and two-dimensional nature as well as its resolution.

Since the present testing and simulation results relate to CG Cu, it is important to assess the applicability of these results to nanostructured materials. As discussed in the introduction, CG Cu was selected as a model material because it displays a large uniform elongation which makes it easier to study the size effect on ductility and especially the uniform elongation. By contrast, nanostructured materials processed by severe plastic deformation were not selected for this investigation because of their small uniform elongations which make it difficult to evaluate the size effect. Despite these limitations, earlier work on nanostructured Cu revealed a similar trend whereby the uniform elongation decreased with decreasing specimen thickness and increasing gauge length when strain was measured from the crosshead displacement (see, for example, Fig. 2 of reference [51]). The post-necking elongation and the elongation to failure decrease evidently with decreasing specimen thickness and increasing gauge length. Thus, these results are in good agreement with the present results obtained from the FEM simulation and experiments using CG Cu. In addition, a similar size effect in which the elongation to failure decreased with decreasing specimen thickness was reported also in a nanocrystalline NiFe alloy prepared using an electrodeposition method [55]. Based on this evidence, it is reasonable to anticipate that the present conclusions, although derived from CG Cu, are equally applicable to nanostructured materials.

5. Conclusions

1. In the absence of accurate strain measurement techniques in tension, such as digital image correlation technique or laser interferometry, the strains derived based on the crosshead displacement may contain serious errors depending on the specimen geometry and size. Thus, both the uniform elongation and the post-necking elongation increase with decreasing gauge length and increasing specimen thickness.
2. The experimental errors in strain measurements from the crosshead displacement are attributed to the contributions of machine compliance of the loading frame and gauge corner deformation, where the latter increases with increasing thickness and decreasing gauge length.

3. The strain measured from the gauge length elongation is influenced by the specimen dimensions so that the post-necking elongation increases with decreasing gauge length and increasing specimen thickness.

4. The results show that the strain is most readily measured from the gauge length elongation and the extent of uniform elongation should be used for comparisons of the tensile ductilities of materials having different dimensions.

5. The results demonstrate it would be advantageous to develop an experimental protocol for testing miniature dog-bone specimens that can be adopted throughout the materials science community. This would minimize measurement errors and provide an opportunity for making meaningful comparisons of experimental data from different laboratories.

Acknowledgements

References

[1] C.C. Koch, D.G. Morris, K. Lu, A. Inoue, MRS Bull. 24 (1999) 54–58.
[2] J.R. Weertman, in: C.C. Koch (Ed.), Nanostructured Materials: Proceeding, Properties and Applications, 2nd ed., William Andrews, Norwich, New York, 2007, pp. 537–564.
[3] C.C. Koch, Scripta Mater. 49 (2003) 657–662.
[4] E. Ma, Scripta Mater. 49 (2003) 663–668.
[5] C.C. Koch, K.M. Youssef, R.O. Scattergood, K.L. Murty, Adv. Eng. Mater. 7 (2005) 787–794, references therein.
[6] E. Ma, JOM 58 (4) (2006) 49–53, references therein.
[7] Y.T. Zhu, X.Z. Liao, Nat. Mater. 3 (2004) 351–352.
[8] Z. Horita, K. Ohashi, T. Fujita, K. Kaneko, T.G. Langdon, Adv. Mater. 17 (2005) 1599–1602.
[9] Y.H. Zhao, X.Z. Liao, S. Cheng, E. Ma, Y.T. Zhu, Adv. Mater. 18 (2006) 2280–2283.
[10] Y.H. Zhao, Y.T. Zhu, X.Z. Liao, Z. Horita, T.G. Langdon, Appl. Phys. Lett. 89 (2006) 121906-1–121906-3.
[11] Y.H. Zhao, J.F. Bingert, X.Z. Liao, B.Z. Cui, K. Han, A. Serhueeva, A.K. Muhkerjee, R.Z. Valiev, T.G. Langdon, Y.T. Zhu, Adv. Mater. 18 (2006) 2494–2498.
[12] X.H. Chen, L. Lu, Scripta Mater. 57 (2007) 133–136.
[13] S. Cheng, Y.H. Zhao, Y.T. Zhu, E. Ma, Acta Mater. 55 (2007) 5822–5832.
[14] K.X. Tao, H. Choo, H.Q. Li, B. Clausen, J.E. Jin, Y.K. Lee, Appl. Phys. Lett. 90 (2007) 101911-1–1101911-3.
[15] Y.H. Zhao, T. Topping, J.F. Bingert, A.M. Dangelewicz, Y. Li, W. Liu, Y.T. Zhu, Y.Z. Zhou, E.J. Lavernia, Adv. Mater. 20 (2008) 3028–3033.
[16] http://www.astm.org.
[17] L. Lu, Y. Shen, X. Chen, L. Qian, K. Lu, Science 304 (2004) 422–425.
[18] K.M. Youssef, R.O. Scattergood, K.L. Murty, J.A. Horton, C.C. Koch, Appl. Phys. Lett. 87 (2005) 091904-1–091904-3.
[19] K.M. Youssef, R.O. Scattergood, K.L. Murty, C.C. Koch, Scripta Mater. 54 (2006) 251–256.
[20] R.Z. Valiev, A.V. Sergueeva, A.K. Mukherjee, Scripta Mater. 49 (2003) 669–674.
[21] A.V. Sergueeva, V.V. Stolyarov, R.Z. Valiev, A.K. Mukherjee, Scripta Mater. 45 (2001) 747–752.
[22] V.L. Tellkamp, A. Melmed, E.J. Lavernia, Metall. Mater. Trans. A32 (2001) 2335–2343.
[23] X.C. Luo, K. Cheng, D. Webb, F. Wardle, J. Mater. Process. Tech. 167 (2005) 515–528.
[24] R. Boden, M. Lehto, U. Simu, G. Thornell, K. Hjort, J.A. Schweitz, Sens. Actuators A127 (2006) 88–93.
[25] B.D. Iverson, S.V. Garimella, Microfluidics Nanofludics 5 (2008) 145–174.
[26] U. Simu, S. Johansson, Sens. Actuators A132 (2006) 632–642.
[27] Y. Qin, J. Mater. Process. Tech. 177 (2006) 8–18.
[28] M.D. Uchic, D.M. Dimiduk, J.N. Florando, W.D. Nix, Science 305 (2004) 986–989.
[29] C.A. Volkert, E.T. Lilleodden, Phil. Mag. 86 (2006) 5567–5579.
[30] J. Biener, A.M. Hodge, J.R. Hayes, C.A. Volkert, L.A. Zepeda-Ruiz, A.V. Hamza, F.F. Abraham, Nano Lett. 6 (2006) 2379–2382.
[31] J.R. Greer, W.C. Oliver, W.D. Nix, Acta Mater. 53 (2005) 1821–1830.
[32] A. Rinaldi, P. Peralta, C. Friesen, K. Sieradzki, Scripta Mater. 56 (2008) 511–514.
[33] X.D. Han, K. Zheng, Y.F. Zhang, X.N. Zhang, Z. Zhang, Z.L. Wang, Adv. Mater. 19 (2007) 2112–2118.
[34] H. Guo, P.F. Yan, Y.B. Wang, J. Tan, Z.F. Zhang, M.L. Sui, E. Ma, Nat. Mater. 6 (2007) 735–739.
[35] W. Liang, M. Zhou, Proc. Instn. Mech. Engs. C218 (2004) 599–606.
[36] D. Kiener, W. Grosinger, G. Dehm, R. Pippan, Acta Mater. 56 (2008) 580–592.
[37] T. Tabata, H. Fujita, S. Yamamoto, T. Cyoji, J. Phys. Soc. JPN 40 (1976) 792–797.
[38] M. Klein, A. Hadrboletz, B. Weiss, G. Khatibi, Mater. Sci. Eng. A319 (2001) 924–928.
[39] A. Hadrboletz, B. Weiss, G. Khatibi, Int. J. Fract. 109 (2001) 69–89.
[40] H.D. Espinosa, B.C. Prorok, B. Peng, J. Mech. Phys. Solids 52 (2004) 667–689.
[41] G. Simons, C. Weippert, J. Dual, J. Villain, Mater. Sci. Eng. A416 (2006) 290–299.
[42] Y. Yang, N. Yao, W.O. Soboyejo, C. Tarquinio, Scripta Mater. 58 (2008) 1062–1065.
[43] Q. Ma, D.R. Clarke, J. Mater. Res. 10 (1995) 853–863.
[44] N.A. Fleck, J.W. Hutchinson, J. Mech. Phys. Solids 41 (1993) 1825–1857.
[45] Z.P. Bazant, S.D. Pang, PNAS 103 (2006) 9434–9439.
[46] H.M. Zbib, E.C. Aifantis, Scripta Mater. 48 (2003) 155–160.
[47] K. Sieradzki, A. Rinaldi, C. Friesen, P. Peralta, Acta Mater. 54 (2006) 4533–4538.
[48] G. Dehm, C. Motz, C. Scheu, H. Clemens, P.H. Mayrhofer, C. Mitterer, Adv. Eng. Mater. 8 (2006) 1033–1045.
[49] G.P. Zhang, C.A. Volkert, R. Schwaiger, P. Wellner, E. Arzt, O. Kraft, Acta Mater. 54 (2006) 3127–3139.
[50] Y. Xiang, J.J. Vlassak, Acta Mater. 54 (2006) 5449–5460.
[51] Y.H. Zhao, Y.Z. Guo, Q. Wei, A.M. Dangelewicz, C. Xu, Y.T. Zhu, T.G. Langdon, Y.Z. Zhou, E.J. Lavernia, Scripta Mater. 59 (2008) 627–630.
[52] A.K. Ghosh, W.A. Backofen, Metall. Trans. 4 (1973) 1113–1123.
[53] G.E. Dieter, Mechanical Metallurgy, McGraw-Hill, New York, 1986.
[54] A.K. Ghosh, Metall. Trans. 5 (1974) 1607–1616.
[55] H. Wei, G.D. Hibbard, G. Palumbo, U. Erb, Scripta Mater. 57 (2007) 996–999.
[56] Y. Kohno, A. Kohyama, M.L. Hamilton, T. Hirose, Y. Katoh, F.A. Garner, J. Nucl. Mater. 283 (2000) 1014–1017.
[57] Y. Ma, T.G. Langdon, Metall. Mater. Trans. A25 (1994) 2309–2311.
[58] K. Decamp, L. Nauvineau, J. Besson, A. Pineau, Inter. J. Fracture 88 (1997) 1–18.
[59] W.N. Sharpe, B. Yuan, R.L. Edwards, J. Microelectromech. Syst. 6 (1997) 193–199.
[60] K.J. Hemker, W.N. Sharpe, Annu. Rev. Mater. Res. 37 (2007) 93–126.
[61] G. Vendroux, W.G. Knauss, Exp. Mech. 38 (1998) 86–92.